$BaMnO_{3-x}$ Revisited: A Structural and Magnetic Study

Josephine J. Adkin and Michael A. Hayward*

Department of Chemistry, Inorganic Chemistry Laboratory, University of Oxford, South Parks Road, Oxford, OX1 3QR England

Received August 30, 2006. Revised Manuscript Received December 5, 2006

The synthesis and structural characterization of 15R-, 8H-, 6H′-, and 10H-$BaMnO_{3-x}$ and 9R-$Ba_{0.875}Sr_{0.125}MnO_3$ is described. Neutron powder diffraction data reveal a strong preference for the location of anion vacancies within the face-shared hexagonal layers of these phases. At high anion vacancy concentrations, Mn_2O_{9-x} dimer units become prevalent. Magnetic characterization indicates antiferromagnetic order in all phases. Ordering temperatures are in the range 250 K < T < 270 K and show a dependence on the fraction of cubic layers present in the stacking sequence.

Introduction

Mixed-valence Mn(III/IV) oxides have attracted considerable attention since the observation of large magnetoresistive ratios in these materials.[1−3] Interest has endured because of the presence of strong coupling between the spin, charge, and lattice degrees of freedom in these phases, which can be modulated as a function of chemical composition.[4,5] Extensive efforts have been directed toward understanding the influence of subtle structural distortions, brought about by compositional changes, on the observed physical properties of phases with arrays of apex-linked MnO_6 octahedra, such as those with the cubic perovskite or Ruddlesden−Popper type structures. Little attention, however, has been directed to the hexagonal perovskite phases, which in addition to apex-sharing, incorporate face-sharing links between MnO_6 octahedra.

The structures adopted by $AMnO_3$ phases (A = electropositive cation) can be rationalized by the structural tolerance factor, t ($t = \langle A-O \rangle / \sqrt{2}\langle Mn-O \rangle$).[6] Compositions with tolerance factors equal to unity have the geometrically ideal ratio of A−O and Mn−O bond lengths to adopt the cubic perovskite structure. Small deviations below unity are accommodated by cooperative twisting and tilting distortions of the MnO_6 octahedra in which the Mn−O−Mn bond angle is reduced below 180° to accommodate small A-site cations. If the tolerance factor takes values greater than unity, hexagonal perovskite structures are adopted in which increasing numbers of face-shared links between MnO_6 octahedra are formed in order to expand the A-cation sites.[7] These face-shared Mn−O−Mn linkages have bond angles of approximately 90°. This different geometry can lead to dramatic differences in super-exchange interactions compared with apex-shared connectivity.[8] The ratio of face-sharing to apex-sharing linkages in hexagonal perovskites is dependent on the size of the tolerance factor as demonstrated by the structural progression of the group 2 $AMnO_3$ manganates. $CaMnO_3$ (t = 0.987) adopts a distorted cubic perovskite structure (all apex-sharing);[9] $SrMnO_3$ (t = 1.033) adopts a 4H structure (1:1 apex: face-sharing);[10] $BaMnO_3$ (t = 1.089) adopts a 2H structure (all face-sharing).[11]

Table 1. Synthetic Conditions Employed for the Preparation of $BaMnO_{3-x}$ Phases

sample	atmosphere	T (°C)	t (h)
15R-$BaMnO_{2.99(1)}$	2:1 argon:oxygen	1330	200
		1335	40
		1345	40
8H-$BaMnO_{2.95(1)}$	2:1 argon:oxygen	1400	80
9R-$Ba_{0.875}Sr_{0.125}MnO_{3.00(1)}$	Air	1000	48 (2 days)
		1050	336 (14 days)
		1100	216 (9 days)
		1150	552 (23 days)
6H′-$BaMnO_{2.92(2)}$	1% oxygen in argon	1300	60
10H-$BaMnO_{2.91(1)}$	1% oxygen in argon	1400	80

The average Mn−O bond length also influences the tolerance factor. This can be adjusted by changing the mean manganese oxidation state, either by A-site doping or through the introduction of anion vacancies. Negas and Roth[12] reported a number of different phases of composition $BaMnO_{3-x}$ with structures in which the ratio of corner-sharing (cubic) to face-sharing (hexagonal) layers is determined by the oxygen stoichiometry. We have previously

* Corresponding author. Tel: 44 1865 272623. Fax: 44 1865 272690. E-mail: michael.hayward@chem.ox.ac.uk.

(1) Chahara, K.; Ohno, T.; Kasao, M.; Kozono, Y. *Appl. Phys. Lett.* **1993**, *63*, 1990.
(2) Schiffer, P.; Ramirez, A. P.; Bao, W.; Cheong, S.-W. *Phys. Rev. Lett.* **1995**, *75*, 3336.
(3) von Helmolt, R.; Wecker, J.; Holzapfel, B.; Schultz, L.; Sanwer, K. *Phys. Rev. Lett.* **1993**, *71*, 2331.
(4) Ibarra, M. R.; Algarabel, P. A.; Biasco, J.; Garcia, J. *Phys. Rev. Lett.* **1995**, *75*, 3541.
(5) Radaelli, P. G.; Marezio, M.; Hwang, H. Y.; Cheong, S.-W.; Batlogg, B. *Phys. Rev. B* **1996**, *54*, 8992.
(6) Goldschmidt, V. M. *Naturwissenschaften* **1926**, *14*, 477.
(7) Dabrowski, D.; Chmaissem, O.; Mais, J.; Kolesnik, S.; Jorgensen, J. D.; Short, S. J. *Solid State Chem.* **2003**, *170*, 154.
(8) Goodenough, J. B. *Magnetism and the Chemical Bond*; Wiley: New York, 1963.
(9) Poeppelmeier, K. R.; Leonowicz, M. E.; Scanlon, J. C.; Longo, J. M.; Yelon, W. B. J. *Solid State Chem.* **1982**, *45*, 71.
(10) Battle, P. D.; Gibb, T. C.; Jones, C. W. J. *Solid State Chem.* **1988**, *74*, 60−66.
(11) Cussen, E. J.; Battle, P. D. *Chem. Mater.* **2000**, *12*, 831−838.
(12) Negas, T.; Roth, R. S. J. *Solid State Chem.* **1971**, *3*, 323.

10.1021/cm062055r CCC: $37.00
Published on Web 01/17/2007

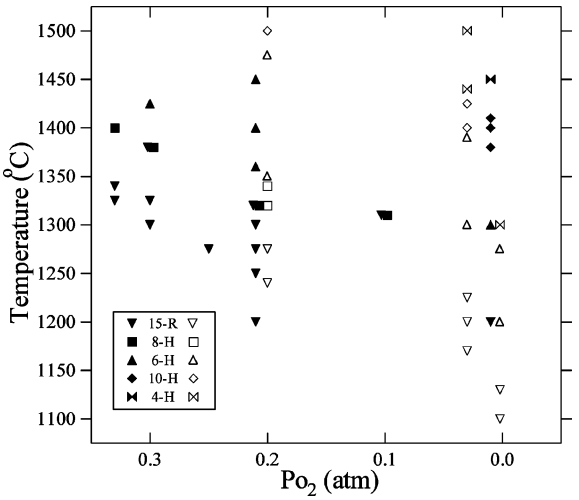

Figure 1. $BaMnO_{3-x}$ phases observed as a function of temperature and P_{O_2}. Open symbols represent data extracted from refs 18 and 19. Closed symbols relate to data in this work.

Table 2. Structural Parameters Refined against Neutron Powder Diffraction Data Collected from 15R-$BaMnO_{2.99(1)}$[a]

atom	*x*	*y*	*z*	fractional occupancy	U_{equiv}
Ba1	0	0	0	1	0.0057(1)
Ba2	0	0	0.13369(5)	1	0.0080(1)
Ba3	0	0	0.26527(4)	1	0.0047(1)
Mn1	0	0	1/2	1	0.0052(1)
Mn2	0	0	0.36177(4)	1	0.0016(1)
Mn3	0	0	0.43157(6)	1	0.0032(1)
O1	1/2	0	0	1	0.0072(1)
O2	0.18603(6)	−0.18603(6)	0.06421(2)	0.9875(1)	0.0051(1)
O3	0.48332(6)	−0.48332(6)	0.13281(2)	1	0.0063(1)

[a] Space group: *R*-3*m*; $a = 5.6791(1)$ Å, $c = 35.345(1)$ Å. $\chi^2 = 2.18$, $wR_p = 3.01\%$, $R_p = 4.90\%$. Titrated stoichiometry = $BaMnO_{2.99(1)}$.

studied the most oxygen deficient of these phases, 4H-$BaMnO_{2.65}$,[13] and observed a strong preference for the location of oxide ion vacancies in the hexagonal layers of this phase, rather than the cubic apex-shared layers. This observation is inconsistent with the structural model proposed by Gonzalez-Calbet and co-workers for the $BaMnO_{3-x}$ series.[14−17] In these studies, Gonzalez-Calbet et al. observed that in the series of $BaMnO_{3-x}$ hexagonal phases, there is a relationship between the relative proportions of hexagonal and cubic layers and the overall stoichiometry of a phase. This can be expressed by the formula: $x = (0.5c)/(h + c)$, where x is the oxygen non-stoichiometry and c and h are the respective numbers of cubic and hexagonal layers in a repeat unit. This leads them to suggest that the most straight forward explanation for this relationship is that the oxide ion vacancies are located in the cubic layers giving them an overall formula of $BaO_{2.5}$, which when stacked with the BaO_3 hexagonal layers gives the observed relationship between composition and structure. We have therefore studied the remaining members of this series to gain a better understanding of anion vacancy locations and magnetic ordering in these phases.

Table 3. Structural Parameters Refined against Neutron Powder Diffraction Data Collected from 8H-$BaMnO_{2.95(1)}$[a]

atom	*x*	*y*	*z*	fractional occupancy	U_{equiv}
Ba1	0	0	0	1	0.0079(1)
Ba2	0	0	1/4	1	0.0094(2)
Ba3	1/3	2/3	0.12839(4)	1	0.0055(1)
Mn1	1/3	2/3	0.55338(5)	1	0.0032(1)
Mn2	1/3	2/3	0.68562(5)	1	0.0041(1)
O1	1/2	0	0	1	0.0070(1)
O2	0.51668(6)	0.0333(1)	1/4	0.979(2)	0.0062(1)
O3	0.81450(3)	0.62899(7)	0.12106(2)	0.977(1)	0.0056(1)

[a] Space group: $P6_3/mmc$; $a = 5.6736(1)$ Å, $c = 18.7550(4)$ Å. χ^2=2.20, $wR_p = 2.34\%$, $R_p = 4.05\%$. Titrated stoichiometry = $BaMnO_{2.95(1)}$.

Table 4. Structural Parameters Refined against Neutron Powder Diffraction Data Collected from 6H′-$BaMnO_{2.92(2)}$[a]

atom	*x*	*y*	*z*	fractional occupancy	U_{equiv}
Ba1	0	0	0	1	0.0056(1)
Ba2	1/3	2/3	1/2	1	0.0109(3)
Ba3	1/3	2/3	0.1667(2)	1	0.0067(1)
Ba4	2/3	1/3	0.3365(1)	1	0.0058(1)
Mn1	0	0	0.2364(1)	1	0.0024(1)
Mn2	0	0	0.4135(2)	1	0.0047(1)
Mn3	2/3	1/3	0.0906(1)	1	0.0041(1)
O1	0.5215(1)	0.4785(1)	0	0.927(6)	0.0045(1)
O2	0.8503(1)	0.8503(1)	1/2	0.952(8)	0.0054(1)
O3	0.8330(1)	0.8330(1)	0.16487(9)	0.998(4)	0.0070(2)
O4	0.1486(1)	0.1486(1)	0.32730(4)	0.984(6)	0.0051(1)

[a] Space group: *P*-6*m*2; $a = 5.6623(1)$ Å, $c = 13.9993(3)$ Å. χ^2=1.74, $wR_p = 2.59\%$, $R_p = 4.91\%$. Refined stoichiometry = $BaMnO_{2.92(2)}$. Titrated stoichiometry = $BaMnO_{2.94(1)}$.

Table 5. Structural Parameters Refined against Neutron Powder Diffraction Data Collected from 10H-$BaMnO_{2.91(1)}$[a]

atom	*x*	*y*	*z*	fractional occupancy	U_{equiv}
Ba1	0	0	1/4	1	0.0056(1)
Ba2	1/3	2/3	0.14939(5)	1	0.0076(1)
Ba3	1/3	2/3	0.54722(4)	1	0.0057(1)
Mn1	0	0	0	1	0.0037(1)
Mn2	0	0	0.10714(4)	1	0.0035(1)
Mn3	1/3	2/3	0.69509(4)	1	0.0044(1)
O1	0.52108(6)	0.0422(1)	1/4	0.933(2)	0.0055(1)
O2	0.14828(4)	0.29655(8)	0.05254(2)	0.984(2)	0.0060(1)
O3	0.83309(5)	0.6662(1)	0.15054(2)	0.979(2)	0.0068(1)

[a] Space group: $P6_3/mmc$; $a = 5.6547(1)$ Å, $c = 23.1936(5)$ Å. χ^2=2.66, $wR_p = 2.36\%$, $R_p = 3.98\%$. Refined stoichiometry = $BaMnO_{2.91(1)}$, titrated stoichiometry = $BaMnO_{2.93(1)}$.

Experimental Section

2H-$BaMnO_3$ was prepared by a standard ceramic route as described by Cussen et al.[11] $BaCO_3$ (99.997%, Alfa Aesar) and MnO_2 (99.999%, Alfa Aesar) were mixed in the appropriate stoichiometric ratio in an agate mortar and then heated at 900 °C in air to decompose the carbonate. The resulting powder was reground and pressed into 13 mm pellets at 5 tons of pressure before being fired at 1000 °C for four periods of 3 days. The sample was reground and repelleted between heating periods.

The $BaMnO_{3-x}$ phase diagram was investigated by annealing samples of well-crystallized 2H-$BaMnO_3$ as a function of temperature and oxygen partial pressure. The use of preformed $BaMnO_3$ removed the need for long-range cation diffusion during the oxygen equilibration process, increasing the rate of reaction and improving the quality of the final products. Oxygen partial pressures in the

(13) Adkin, J. J.; Hayward, M. A. J. *Solid State Chem.* **2006**, *179*, 70.
(14) Gonzalez-Calbet, J. M.; Parras, M.; Alonso, J. M.; Vallet-Regi, M. J. *Solid State Chem.* **1993**, *106*, 99−110.
(15) Gonzalez-Calbet, J. M.; Parras, M.; Alonso, J. M.; Vallet-Regi, M. J. *Solid State Chem.* **1994**, *111*, 202−207.
(16) Parras, M.; Alonso, J. M.; Gonzalez-Calbet, J. M.; Vallet-Regi, M. J. *Solid State Chem.* **1995**, *117*, 21−29.
(17) Parras, M.; Gonzalez-Calbet, J. M.; Alonso, J. M.; Vallet-Regi, M. J. *Solid State Chem.* **1994**, *113*, 78−87.

Table 6. Structural Parameters Refined against Neutron Powder Diffraction Data Collected from 9R-$Ba_{0.875}Sr_{0.125}MnO_{3.00}$

atom	*x*	*y*	*z*	fractional occupancy	U_{equiv}
Ba1/Sr1	0	0	0	0.77(1)/0.23(1)	0.0066(2)
Ba2/Sr2	0	0	0.21939(3)	0.926(5)/0.074(5)	0.0060(2)
Mn1	0	0	1/2	1	0.0033(1)
Mn2	0	0	0.38173(4)	1	0.0033(1)
O1	1/2	0	0	1	0.0074(1)
O2	0.14867(3)	−0.14867(3)	0.55830(2)	1	0.0058(1)

[a] Space group: *R*-3*m*; $a = 5.6397(1)$ Å, $c = 20.8973(6)$ Å. χ^2=3.934, $wR_p = 2.81\%$, $R_p = 4.76\%$. Titrated stoichiometry = $Ba_{0.875}Sr_{0.125}MnO_{3.00(1)}$.

Table 7. Selected Bond Length and Angles Extracted from the Structure of 15R-$BaMnO_{2.99}$

bond	bond length (Å)/angle (deg)
Ba1−O1	2.83956(8)
Ba1−O2	2.9153(7)
Ba2−O2	3.062(2)
Ba2−O3(3×)	2.972(2)
Ba2−O3(6×)	2.84445(9)
Ba3−O1	2.911(1)
Ba3−O2	2.8492(1)
Ba3−O3	2.914(1)
Mn1−O3	1.8999(6)
Mn2−O1	1.9229(8)
Mn2−O2	1.923(1)
Mn3−O2	1.882(2)
Mn3−O3	1.917(2)
Mn1−Mn3	2.420(2)
Mn2−Mn3	2.466(3)
Mn1−O3−Mn3	78.71(5)
Mn2−O2−Mn3	80.77(6)

Table 8. Selected Bond Lengths and Angles Extracted from the Structure of 8H-$BaMnO_{2.95(1)}$

bond	bond length (Å)/angle (deg)
Ba1−O1	2.83680(5)
Ba1−O3	2.9117(4)
Ba2−O2	2.84153(6)
Ba2−O3	3.0285(4)
Ba3−O1	2.9122(7)
Ba3−O2	2.9065(8)
Ba3−O3	2.84616(7)
Mn1−O1	1.9195(5)
Mn1−O3	1.9291(7)
Mn2−O2	1.9054(8)
Mn2−O3	1.8912(7)
Mn1−Mn2	2.480(1)
Mn2−Mn2	2.415(2)
Mn1−O3−Mn2	80.96(3)
Mn2−O2−Mn2	78.65(5)

range 1 atm > P_{O_2} > 0.1 atm were obtained by mixing oxygen (99.5%) and argon (99.998%) prior to passing them over samples. When lower P_{O_2} conditions were required, a certified mixture of 1% (±0.05%) oxygen in argon was used.

Samples of approximately 3 g in mass labeled 15R, 8H, 6H′, and 10H were prepared by annealing 2H-$BaMnO_3$ samples under the conditions described in Table 1. After the final heat treatment, all of the samples were allowed to cool to room temperature under the reaction atmosphere. 9R-$Ba_{0.875}Sr_{0.125}MnO_3$ was prepared from suitable stoichiometric ratios of $BaCO_3$, $SrCO_3$, and MnO_2, which were thoroughly mixed before the carbonates were decomposed by heating at 900 °C in air. The sample was pressed into pellets that were fired as described in Table 1 with intermittent regrinding and repelleting.

Neutron powder diffraction data suitable for structural refinement were collected from all samples at both room temperature and 2 K using the POLARIS instrument at ISIS, U.K. An additional data set was collected from the 6H′ sample at 200 K using the D2B diffractometer at the ILL, Grenoble, France. Structural refinement was carried out using the GSAS suite of programs.[18] Magnetization

Table 9. Selected Bond Lengths and Angles Extracted from the Structure of 6H′-$BaMnO_{2.92(2)}$

bond	bond length (Å)/angle (deg)
Ba1−O1	2.8390(1)
Ba1−O3	2.830(1)
Ba2−O2	2.8361(1)
Ba2−O4	3.0210(8)
Ba3−O1	2.975(2)
Ba3−O3	2.83129(7)
Ba3−O4	2.887(2)
Ba4−O2	2.912(2)
Ba4−O3	2.904(2)
Ba4−O4	2.8396(1)
Mn1−O3	1.920(2)
Mn1−O4	1.935(2)
Mn2−O2	1.903(2)
Mn2−O4	1.893(2)
Mn3−O1	1.908(2)
Mn3−O3	1.934(2)
Mn3−Mn3	2.538(4)
Mn1−Mn2	2.480(4)
Mn2−Mn2	2.422(5)
Mn1−O4−Mn2	80.75(9)
Mn3−O1−Mn3	83.4(1)
Mn2−O2−Mn2	79.0(1)

Table 10. Selected Bond Lengths and Angles Extracted from the Structure of 10H-$BaMnO_{2.91(1)}$

bond	bond length (Å)/angle (deg)
Ba1−O1	2.83489(8)
Ba1−O3	2.8275(4)
Ba2−O1	2.971(1)
Ba2−O2	2.886(1)
Ba2−O3	2.82751(6)
Ba3−O2(6×)	2.83578(8)
Ba3−O2(3×)	2.9393(8)
Ba3−O3	2.8979(9)
Mn1−O2	1.8959(4)
Mn2−O2	1.9268(8)
Mn2−O3	1.9199(7)
Mn3−O1	1.9118(8)
Mn3−O3	1.9298(8)
Mn3−Mn3	2.547(2)
Mn1−Mn2	2.4865(1)
Mn1−O2−Mn2	81.09(3)
Mn3−O1−Mn3	83.54(5)

data were collected using a Quantum Design MPMS SQUID magnetometer in an applied field of 100 Oe after cooling in both zero field and the measuring field. Field-cooled magnetization-field isotherms were collected between ±5 T in the temperature range 5 K < *T* < 300 K. Average manganese oxidation states in all phases were determined by dissolving samples in HCl containing an excess of KI and titrating the liberated I_2 with $Na_2S_2O_3$.

Results

Investigation of the $BaMnO_{3-x}$ phase diagram as a function of temperature and oxygen partial pressure yielded results

(18) Larson, A. C.; Von Dreele, R. B. *General Structure Analysis System*; LANL Report LAUR 86-748; Los Alamos National Laboratory: Los Alamos, NM, 2004.

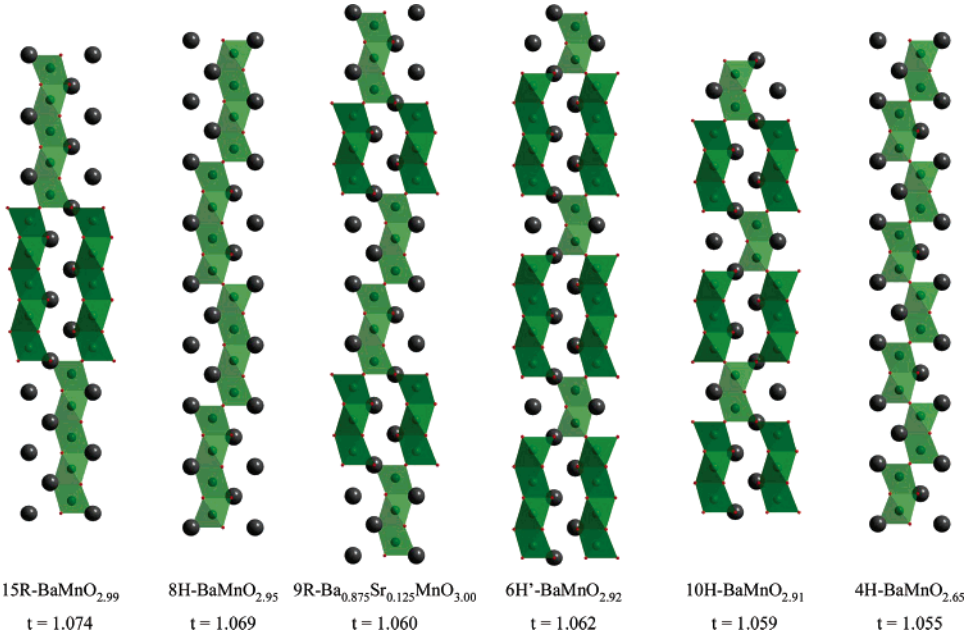

Figure 2. Stacking sequences and tolerance factors of Ba(Sr)MnO_{3-x} phases refined from neutron powder diffraction data.

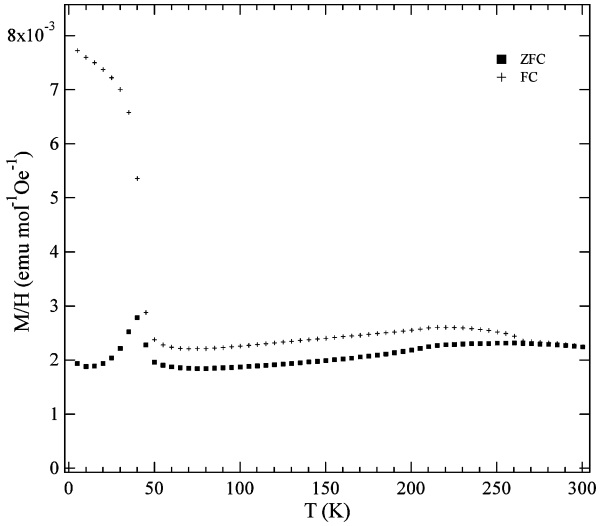

Figure 3. Zero-field-cooled and field-cooled magnetization data collected from 9R-$Ba_{0.875}Sr_{0.125}MnO_{3.00}$.

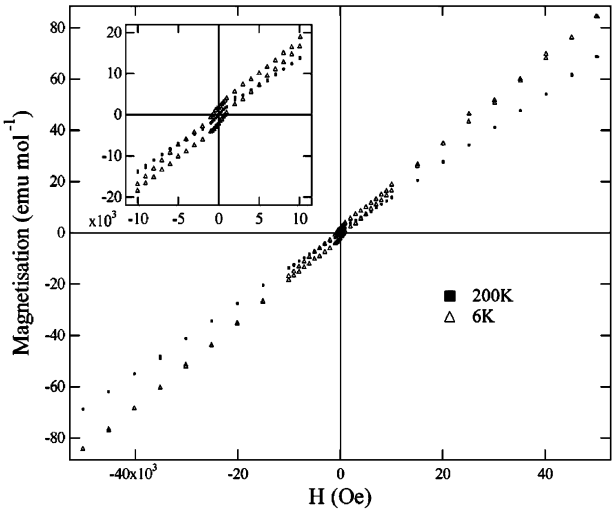

Figure 4. Magnetization data collected as a function of field from 9R-$Ba_{0.875}Sr_{0.125}MnO_{3.00}$.

consistent with previous reports by Negas and Roth[19] (under air) and following the trends reported by Uematsu et al.[20] (under reducing conditions) as shown in Figure 1. The only significant difference was the inability to obtain a single-phase eight-layer sample in oxygen partial pressures equal to or less than air; samples always contained quantities of the 15R phase. Single-phase samples with eight-layer structures could, however, be readily prepared under more oxidizing conditions (P_{O_2} = 0.33 atm, 1400 °C).

The 15R and 9R samples required long heating periods to produce highly ordered crystalline materials (Table 1). X-ray powder diffraction patterns consistent with the described phases were seen after brief heating periods; however, significant anisotropic broadening of *hkl* reflections with respect to *hk*0 reflections was observed in combination with asymmetric peak profiles. These features are consistent with disorder in layered or low-dimensional structures and suggest that the samples contained disordered intergrowths of different $BaMnO_{3-x}$ phases. On prolonged heating, these signatures of disorder diminished so as to become undetectable by high-resolution powder X-ray diffraction; however, very slight peak width anisotropy is observed in the neutron

Table 11. Selected Bond Lengths and Angles Extracted from the Structure of 9R-$BaMnO_{3.00(1)}$

bond	bond length (Å)/angle (deg)
Sr/Ba1−O1	2.81986(7)
Sr/Ba1−O2	2.8952(3)
Sr/Ba2−O1	2.8844(6)
Sr/Ba2−O2(3x)	2.9388(5)
Sr/Ba2−O2(6x)	2.82772(8)
Mn1−O2	1.8956(3)
Mn2−O1	1.9166(4)
Mn2−O2	1.9183(6)
Mn1−Mn2	2.4715(7)
Mn1−O2−Mn2	80.79(2)
Mn2−O1−Mn2	180.000(0)

(19) Negas, T.; Roth, R. S. J. *Solid State Chem.* **1971**, *3*, 323−39.
(20) Uematsu, K.; Kuroda, K.; Mizutani, N.; Kato, M. *J. Am. Ceram. Soc.* **1977**, *60*, 466−477.

powder diffraction data, which was modeled by incorporating an anisotropic broadening axis parallel to 001 into the structural models.

Structural models based on those reported by Negas and Roth[12] were refined against neutron powder diffraction data collected from the 15R, 8H, 6H′, and 10H samples. Atomic coordinates and thermal displacement parameters were refined for all atoms. Particular attention was paid to the fractional occupancies of oxide ions in these phases. Free refinement of the oxygen occupation numbers for the 6H′ and 10H models yielded overall stoichiometries in good agreement with those obtained via iodometric titration. The refinements against data collected from the 15R and 8H samples yielded unrealistically low oxygen occupancies and so these models were constrained such that the total stoichiometry was consistent with the values obtained chemically.

A 9R model based on that described by Chamberland et al.[21] for $BaMnO_{3.00}$ prepared under pressure was used as a starting model for refinement against the data collected from $Ba_{0.875}Sr_{0.125}MnO_3$. Atomic coordinates and thermal displacement parameters were refined, as was the distribution of strontium over the two A-cation sites, constrained only by the total cation stoichiometry. Iodometric titration indicated that the sample was fully oxygen stoichiometric, so oxygen occupancies were fixed at unity.

Refined structural parameters and selected bond lengths are listed in Tables 2−11 . Figure 2 shows the stacking sequences of the structures refined for $Ba(Sr)MnO_{3-x}$ phases. Complete descriptions of the anisotropic thermal displacement parameters and plots of the observed calculated and difference curves for the structural refinements are given in the Supporting Information.

Magnetization data collected from $Ba(Sr)MnO_{3-x}$ samples as a function of temperature all show the same form. Weak, largely temperature-independent susceptibilities were observed in the range 270 K < T < 300 K. Below this temperature range, the zero-field-cooled and field-cooled data diverge but continue to exhibit weak temperature dependence, until at $T \approx 50$ K there is a significant increase in the field-cooled magnetization. Data collected from 9R-$Ba_{0.875}Sr_{0.125}MnO_{3.00}$ are shown in Figure 3 as a typical data set. Figure 4 shows magnetization-field isotherms collected from 9R-$Ba_{0.875}Sr_{0.125}MnO_{3.00}$ at 200 and 5 K. The data collected at 300 K are linear and pass through the origin, consistent with paramagnetic behavior. The data collected at 200 and 6 K show nonlinear behavior, with significant hysteresis in the 6 K data set. Magnetization data collected from the remaining $BaMnO_{3-x}$ phases can be found in the Supporting Information.

The only significant deviation from the behavior described was observed for 15R-$BaMnO_{2.99}$ (Figure 5). For this phase, the field-cooled magnetization data show significant temperature dependence in the intermediate temperature range 50 K < T < 260 K, such that the field-cooled and zero-field-cooled data cross at $T \approx 80$ K; the field-cooled data have a lower absolute magnitude than the zero-field-cooled data below this temperature. This observation suggests ferrimagnetic behavior and is presumably associated with the presence of low levels of disordered intergrowths of other $BaMnO_{3-x}$ phases as suggested by diffraction data. Further evidence for this assertion is provided by the observation that magnetization data collected from 9R-$Ba_{0.875}Sr_{0.125}MnO_{3.00}$ samples after only brief heating showed a form similar to that of the 15R sample (Figure 6), which evolved to the data shown in Figure 3 as the crystallinity of the sample improved. Further heating of the 15R-$BaMnO_{2.99}$ sample, however, did not lead to an observable change in magnetic behavior, suggesting that under the synthesis conditions employed, it is not possible to prepare a perfectly ordered sample of the 15R phase.

Neutron powder diffraction data collected from samples at 2K showed additional diffraction features with respect to the 300 K data sets, for all $Ba(Sr)MnO_{3-x}$ phases. This additional scattering was assigned to the presence of long-range magnetic order. Magnetic models in which the interactions between neighboring manganese centers were

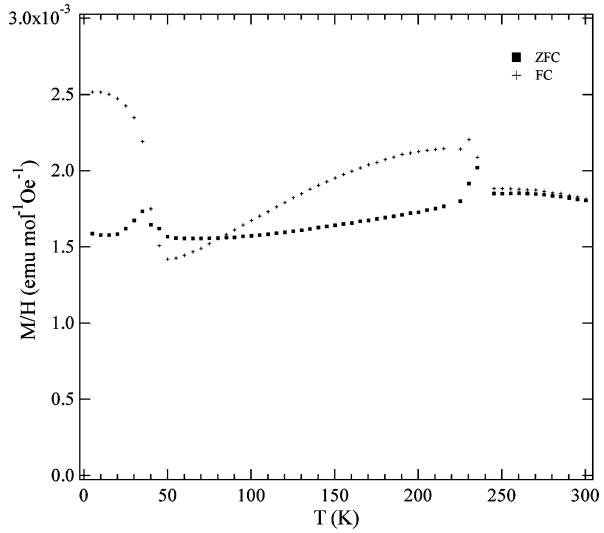

Figure 5. Zero-field-cooled and field-cooled magnetization data collected from 15R-$BaMnO_{2.99}$.

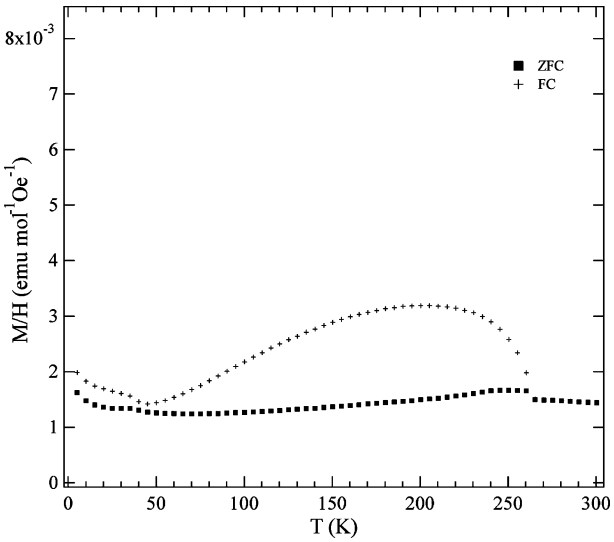

Figure 6. Zero-field-cooled and field-cooled magnetization data collected from poorly crystallized 9R-$Ba_{0.875}Sr_{0.125}MnO_{3.00}$.

(21) Chamberland, B. L.; Sleight, A. W.; Weiher, J. F. J. *Solid State Chem.* **1970**, *1*, 506−511.

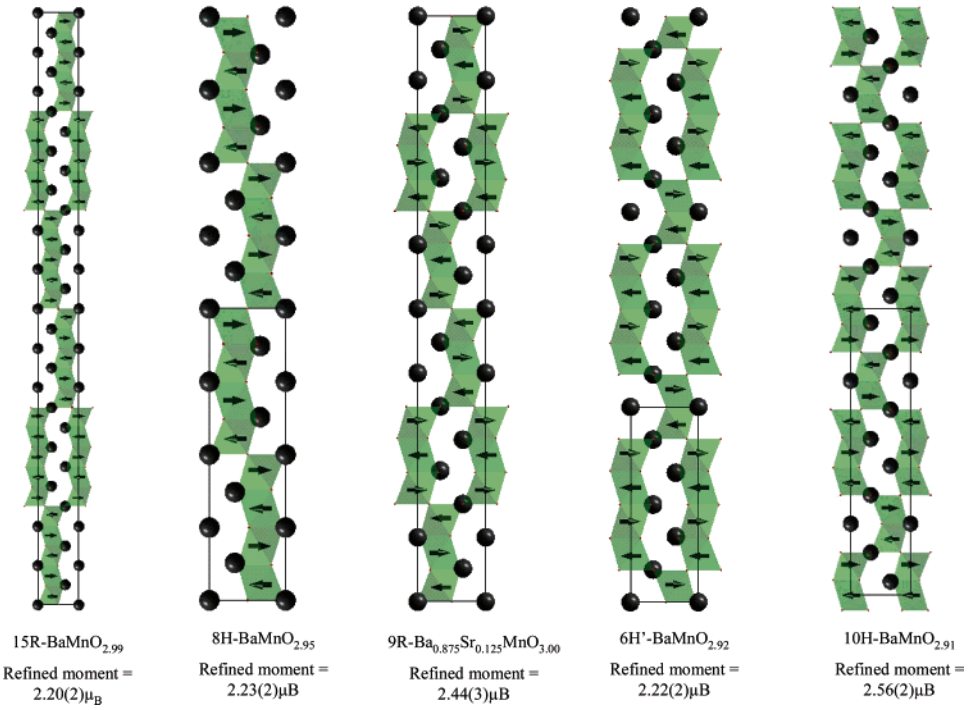

Figure 7. Magnetic structures and ordered magnetic moments of Ba(Sr)MnO_{3-x} phases refined from neutron powder diffraction data collected at 2 K.

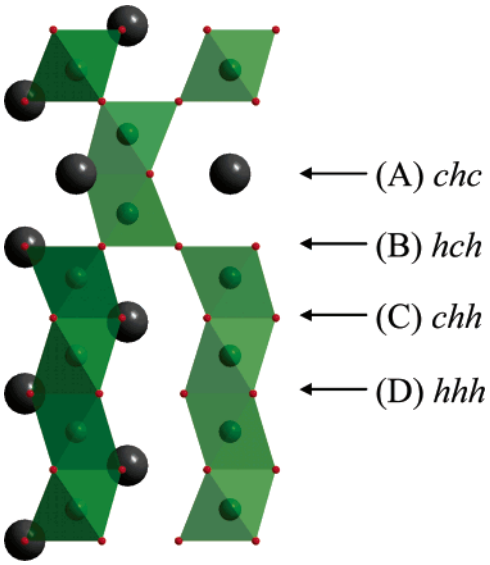

Figure 8. The different anion locations present in hexagonal $BaMnO_{3-x}$ phases.

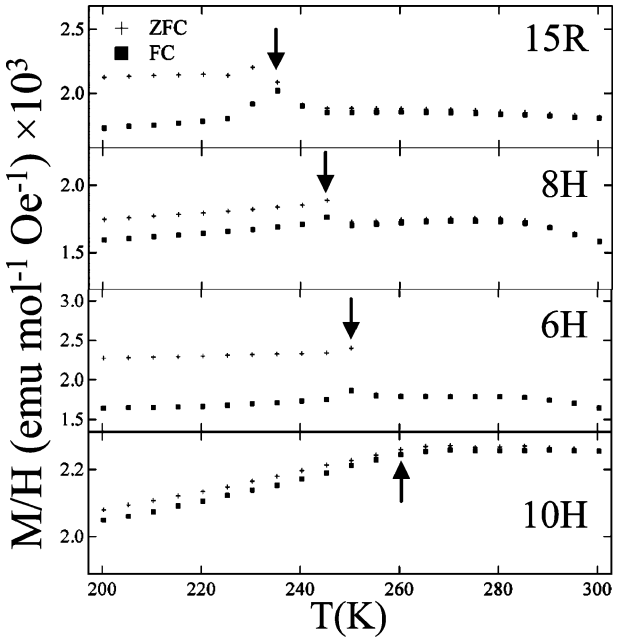

Figure 9. Zero-field-cooled and field-cooled magnetization data collected from $BaMnO_{3-x}$ phases. Arrows highlight features in the data that indicate the onset of long-range antiferromagnetic order.

constrained to be antiferromagnetic by analogy to the ordered magnetic structure observed for 4H-$BaMnO_3$,[13] were refined against these data, and good agreement was achieved in all cases. Figure 7 shows a graphical representation of the refined magnetic structures. Full details of the structural and magnetic refinements against the 2 K neutron powder diffraction data are given in the Supporting Information. Inspection of an additional neutron diffraction data set collected from the 6H′ sample at 200 K revealed that additional magnetic diffraction features were still present at this temperature. Structural refinement of the same magnetic ordering model that was utilized at 2 K resulted in a good fit to the data, but with a reduction in the size of the ordered magnetic moment (1.85(4) μ_B at 200 K as opposed to 2.22-(2) μ_B at 2 K).

Discussion

Structures. High-resolution neutron powder diffraction experiments have confirmed the cation structures reported for the series $BaMnO_{3-x}$ by Negas and Roth[19] and allowed the accurate location of the oxygen anions and anion vacancies to be determined. Using these values to calculate the structural tolerance factors for each phase reveals that, as expected, the fraction of cubic layers in stacking sequence increases as the structural tolerance factor decreases (Figure 2). Thus, the substitution of strontium for barium and/or reduction of the manganese via the introduction of anion vacancies results in a greater proportion of cubic layers in

Table 12. Barium−Oxygen Bond Lengths (Å) for the Different Anion Locations in $BaMnO_{3-x}$ Phases (values for 4H-$BaMnO_{3-x}$ were extracted from ref 13)

anion site	bond	15R	8H	6H′	10H	4H
chc (A)	Ba in			2.839	2.835	2.851
	Ba out_c			2.975	2.971	2.992
	Ba out_c			2.975	2.971	2.992
	average			2.907	2.903	2.921
hch (B)	Ba in	2.840	2.837	2.831	2.828	2.842
	Ba out_h	2.911	2.912	2.904	2.899	2.857
	Ba out_h	2.911	2.912	2.830	2.827	2.857
	average	2.876	2.875	2.849	2.846	2.850
hhc (C)	Ba in	2.849	2.846	2.840	2.836	
	Ba out_h	3.063	3.028	3.021	2.939	
	Ba out_c	2.915	2.912	2.887	2.886	
	average	2.919	2.908	2.897	2.874	
hhh (D)	Ba in	2.844	2.842	2.836		
	Ba out_h	2.972	2.907	2.912		
	Ba out_h	2.844	2.907	2.912		
	average	2.876	2.875	2.874		

the unit cell. This structural relation is expected by analogy to other hexagonal perovskite phases.

Close inspection of the structures refined for the different $BaMnO_{3-x}$ phases reveals a strong preference for the location of anion vacancies with the hexagonally stacked layers rather than the cubic layers. This observation is consistent with previous neutron powder diffraction studies of 4H-$BaMnO_{3-x}$ and 4H-(Ba/Sr)MnO_{3-x}[13,22] but strongly contradicts the structural model proposed by Gonzalez-Calbet and co-workers, based on electron diffraction data.[14−17] In addition, the oxygen stoichiometries of $BaMnO_{3-x}$ phases measured in this study do not follow the required simple formula they proposed.

The preferential location of oxide ion vacancies within the hexagonally stacked layers of $BaMnO_{3-x}$ phases can be rationalized by examining the different coordination environments adopted by oxide ions in these structures, particularly the barium-oxygen bonds. Although the manganese−oxygen interactions will have some influence of the location of anion vacancies, it is presumed that the much more electropositive barium ion will have a dominant influence, as has been observed in other anion-deficient manganese phases.[23]

There are four different environments that are adopted by oxide ions (Figure 8): the central layer of a *chc* stack (A); the central layer of an *hch* stack (B); the central layer of an *hhc* stack (C); and the central layer of an *hhh* stack (D). The barium−oxygen bond lengths for the four different anion locations are listed in Table 12. Calculating the average barium−oxygen bond length for each site reveals that oxide ions within cubic layers have the shortest (or equal shortest in the case of the 15R and 8H structures) bonds, indicating the strongest bonding interaction. Thus, the removal of these oxide ions would result in the largest loss of lattice energy, compared to the removal of oxide ions from other sites. This observation provides a simple explanation for the lack of oxygen vacancies in cubic layers and suggests it is a general feature of anion-deficient hexagonal manganese oxides.

The anion vacancies in $BaMnO_{3-x}$ phases also have a structure-directing effect on the stacking sequences adopted. Examination of the refined structures of Ba(Sr)MnO_{3-x} phases suggests they can be separated into two classes. In phases where there are relatively few anion vacancies (15R, 8H, 9R), this structure-directing effect is minimal above the obvious influence on the average manganese oxidation state and thus the structural tolerance factor. It would seem reasonable to expect the cubic layers within these phases to be distributed evenly through the structure, on the basis of packing arguments, and this is indeed what is observed. As the concentration of anion vacancies increases (6H′, 10H, 4H), a different behavior is observed. Mn_2O_{9-x} units become prevalent in the stacking sequence. Examination of the average barium−oxygen bond lengths for the different anion environments listed in Table 12 reveals that the hexagonal layers in the center of Mn_2O_{9-x} dimers (*chc* site) have by far the longest barium oxygen bonds. Utilizing the arguments discussed previously, this indicates this is the most favorable position to accommodate an anion vacancy. It can thus be seen that the increasing concentration of anion vacancies drives a change in the stacking sequence of $BaMnO_{3-x}$ phases, favoring the formation of *chc* repeats. This effect can be seen clearly by comparing the structures of 9R-$Ba_{0.875}Sr_{0.125}MnO_{3.00}$ and 6H′-$BaMnO_{2.92}$. These two phases have very similar tolerance factors (1.060 vs 1.062) and thus identical ratios of cubic and hexagonal layers (1:2), but only the 6H′ phase contains anion vacancies. This results in the adoption of different stacking sequences for the two phases. $Ba_{0.875}Sr_{0.125}MnO_{3.00}$ adopts the 9R structure with a simple *chhchh* stacking sequence, which maximizes the separation between cubic layers. $BaMnO_{2.92}$, however, adopts the 6H′ structure with a more complex *chchhh* stacking sequence so as to incorporate a favorable *chc* stacking repeat to accommodate the large concentration of anion vacancies present.

Magnetism. The magnetic susceptibility data collected from Ba(Sr)MnO_{3-x} phases are reminiscent of the analogous data collected from 4H-$BaMnO_{2.65}$ and 4H-$SrMnO_{3.10}$.[13] In these latter examples, the magnetization data have a very small absolute value and a small temperature dependence, with no evidence of long-range magnetic order at 300 K. However, at low-temperature, neutron diffraction data show they adopt three-dimensionally ordered magnetic structures with ordered moments of magnitude consistent with $s = {}^3/_2$-Mn(IV). These apparently contradictory observations are reconciled by a model in which the magnetic moments of manganese are antiferromagnetically coupled, but not three-dimensionally ordered, at room temperature. On cooling, full three-dimensional order is observed to take place in 4H-$SrMnO_3$ at 278 K. However, this ordering transition has no signature in the magnetization data, as the total number of antiparallel aligned spins does not change, just their relative orientation.[10] Similar behavior is observed for 4H-$BaMnO_{3-x}$ and 4H-$Ba_{0.5}Sr_{0.5}MnO_{3-x}$.[13] In the latter example, a small divergence between zero-field-cooled and field-cooled magnetization data is observed at the ordering temperature; we propose a similar model for the $BaMnO_{3-x}$ phases described here. Figure 9 plots the high-temperature region of the magnetization data collected from $BaMnO_{3-x}$ samples. It can be seen that the anomaly which we assign to the onset of magnetic order in each phase increases steadily with *x*, and

(22) Jacobson, A. J.; Horrox, A. J. W. *Acta Crystallogr., Sect. B* **1976**, *32*, 1003−8.
(23) Hayward, M. A. *Chem. Mater.* **2006**, *18*, 321.

thus the fraction of cubic layers within the structures. This observation is consistent with the idea that the strong antiferromagnetic coupling between spins is mediated by the ~90° Mn−O−Mn links, which are formed by the face-sharing of MnO_6 octahedra, with full three-dimensional ordering occurring only when the weaker ~180° Mn−O−Mn superexchange pathway formed by the corner sharing of MnO_6 octahedra can overcome thermal scattering. In this model, it would be expected that the ordering transition temperature would scale with the relative fraction of cubic layers, as is observed. Support for this high-temperature ordering model is provided by the observation of full three-dimensional magnetic order in the 6H′ sample at 200 K via neutron diffraction.

The large divergence between the zero-field-cooled and field cooled data at $T \approx 50$ K in all samples is thought to be a spin-canting transition. Similar transitions are observed in 4H-$BaMnO_{3-x}$ and 4H-$Ba_{0.5}Sr_{0.5}MnO_{3-x}$,[13] and the transition temperature is similar to the Néel temperature of 2H-$BaMnO_3$.[11] 2H-$BaMnO_3$ has a structure that contains no cubic stacked layers and thus the face-shared columns of MnO_6 octahedra are isolated from each other. The observation of magnetic order at a relatively high temperature in this phase demonstrates appreciable interchain magnetic coupling in the absence of cross links formed by corner sharing. We propose that this interchain coupling pathway, which presumably utilizes barium orbitals, is the origin of this canting transition observed in hexagonal Ba(Sr)MnO_{3-x} phases and indeed many other low dimensional barium manganese oxides.

Acknowledgment. We thank R. Smith and E. Suard for assistance in collecting the neutron powder diffraction data and the EPSRC and Royal Society for funding.

Supporting Information Available: Observed, calculated, and difference plots and a complete description of anisotropic thermal parameters for the structural refinements of all phases at 300 K. Magnetization data collected from 8H, 6H′ and 10H $BaMnO_3$. Observed, calculated, and difference plots and full structural details of the structural refinements of all phases at 2 K and 6H′ at 200 K. This material is available free of charge via the Internet at http://pubs.acs.org.

CM062055R